

Observation of three-photon bound states in a quantum nonlinear medium

Qi-Yu Liang¹, Aditya V. Venkatramani², Sergio H. Cantu¹, Travis L. Nicholson¹, Michael J. Gullans^{3,4}, Alexey V. Gorshkov⁴, Jeff D. Thompson⁵, Cheng Chin⁶, Mikhail D. Lukin², and Vladan Vuletić¹

¹Department of Physics and Research Laboratory of Electronics, Massachusetts Institute of Technology, Cambridge, Massachusetts 02139, USA

²Department of Physics, Harvard University, Cambridge, Massachusetts 02138, USA

³Department of Physics, Princeton University, Princeton, New Jersey 08544, USA

⁴Joint Quantum Institute and Joint Center for Quantum Information and Computer Science, National Institute of Standards and Technology and University of Maryland, College Park, Maryland 20742, USA

⁵Department of Electrical Engineering, Princeton University, Princeton, NJ 08544, USA

⁶James Franck Institute, Enrico Fermi Institute and Department of Physics, University of Chicago, Chicago, IL 60637, USA

Bound states of massive particles, such as nuclei, atoms or molecules, constitute the bulk of the visible world around us. In contrast, photons typically only interact weakly. We report the observation of traveling three-photon bound states in a quantum nonlinear medium where the interactions between photons are mediated by atomic

Rydberg states. Photon correlation and conditional phase measurements reveal the distinct bunching and phase features associated with three-photon and two-photon bound states. Such photonic trimers and dimers possess shape-preserving wavefunctions that depend on the constituent photon number. The observed bunching and strongly nonlinear optical phase are quantitatively described by an effective field theory (EFT) of Rydberg-induced photon-photon interactions, consistent with the presence of a substantial effective three-body force between the photons. These observations demonstrate the ability to realize and control strongly interacting quantum many-body states of light.

Bound states of light quanta have been proposed to exist in specifically engineered media with strong optical nonlinearities (1–5). Recently photonic dimers have been observed experimentally (6). Such bound states of photons can be viewed as quantum solitons (7, 8), which are shape-preserving wave-packets enabled by the cancellation of nonlinear and dispersive effects. In contrast to classical solitons where the self-consistent shape varies smoothly with total pulse energy, in a quantum soliton the optical nonlinearity is so strong that the wave packet shape depends on the constituent number of photons in a quantized manner (7, 8). The creation of quantum solitons not only represents an important step in fundamental studies of photonic quantum matter (6, 9, 10), but also may enable new applications in areas ranging from quantum communication to quantum metrology (11, 12).

We search for a photonic trimer using an ultracold atomic gas as a quantum nonlinear medium. This medium is experimentally realized by coupling photons to highly excited atomic Rydberg states by means of electromagnetically induced transparency (EIT). The

resulting hybrid excitations of light and matter – Rydberg polaritons – inherit strong interactions from their Rydberg components, and can propagate with very low loss at slow group velocity v_g (13–15). The nonlinearity arises when photons are within a Rydberg blockade radius r_B of one another, where strong interactions between atoms in the Rydberg state (16) shift the Rydberg level out of the EIT resonance, blocking the excitation of more than one Rydberg atom within r_B . In the dissipative regime (on atomic resonance), the blockade results in photon loss and anti-bunching (17–19). In the dispersive, off-resonant regime, the index of refraction varies with the separation between photons, resulting in an attractive force (6).

Our experimental setup (20) (Fig 1A, B) consists of a weak quantum probe field at 780 nm coupled to the $100S_{1/2}$ Rydberg state via a strong 479 nm control field in the EIT configuration (see Fig. 1B). The interactions occur in a cloud of laser-cooled ^{87}Rb atoms in a far-detuned optical dipole trap. The system is effectively one-dimensional for the photons, due to the blockade radius ($r_B = 20\ \mu\text{m}$) being large compared to the transverse extent of the probe beam waist ($w=4.5\ \mu\text{m}$), but smaller than the atomic cloud along the propagation direction ($\sim 130\ \mu\text{m}$). Measurements are conducted at a peak optical depth per blockade radius $\text{OD}_B \simeq 5$. To suppress dissipative effects, we work at large detuning $\Delta \geq 3\Gamma$ from atomic resonance (Γ is the population decay rate of the $5P_{3/2}$ state, see Fig. 1B), and at a control laser Rabi frequency where the transmission through the medium is the same with and without EIT, but the phase differs appreciably (Fig. 1C). Consequently, the transmission hardly varies with probe photon rate (Fig. 1D top), while a strongly rate-dependent phase with a slope of $0.40(7)\ \text{rad}\cdot\mu\text{s}$ is observed (Fig. 1D bottom).

The quantum dynamics of interacting photons are investigated by measuring the three-photon correlation function and phase. Because dispersion outside of the atomic medium

is negligible, any amplitude and phase features formed inside the nonlinear medium are preserved outside, and can be detected in the form of photon number and phase correlations. The third-order photon correlation function has been measured previously in coupled atom-cavity and quantum dot-cavity systems, as well as in non-classical states of three photons such as the Greenberger-Horne-Zeilinger (GHZ) and ‘N00N’ states (12). In our approach, we split the light onto three single-photon counting modules. Furthermore, by mixing a detuned local oscillator (LO) into the final beamsplitter, we can also perform a heterodyne measurement in one of the detection arms (Fig. 1A). To connect the observed correlations to the physics of interacting Rydberg polaritons, we consider a state containing up to three photons,

$$|\psi\rangle = |0\rangle + \int dt_1 \psi_1(t_1)|t_1\rangle + \int dt_1 dt_2 \psi_2(t_1, t_2)|t_1, t_2\rangle + \int dt_1 dt_2 dt_3 \psi_3(t_1, t_2, t_3)|t_1, t_2, t_3\rangle, \quad (1)$$

where $|t_1, \dots, t_N\rangle = \frac{1}{N!} a^\dagger(t_1) \dots a^\dagger(t_N) |0\rangle$, and $a^\dagger(t)$ is the photon creation operator of the time bin mode t . The correlation functions can be related to the wavefunctions as $g^{(2)}(t_1, t_2) = \frac{|\psi_2(t_1, t_2)|^2}{|\psi_1(t_1)|^2 |\psi_1(t_2)|^2}$ and $g^{(3)}(t_1, t_2, t_3) = \frac{|\psi_3(t_1, t_2, t_3)|^2}{|\psi_1(t_1)|^2 |\psi_1(t_2)|^2 |\psi_1(t_3)|^2}$. We refer to the phase $\tilde{\phi}^{(N)}$ of the N -photon wavefunction ψ_N as the N -photon phase, namely, $\tilde{\phi}^{(1)}(t_1) = \text{Arg}[\psi_1(t_1)]$, $\tilde{\phi}^{(2)}(t_1, t_2) = \text{Arg}[\psi_2(t_1, t_2)]$, and $\tilde{\phi}^{(3)}(t_1, t_2, t_3) = \text{Arg}[\psi_3(t_1, t_2, t_3)]$. The N -photon phase is obtained from the phase of the beat note signal on the third detector, conditioned on having observed $N-1$ photons in the other two detectors. The conditional phase relative to N uncorrelated photons, i.e. the nonlinear part of the phase, is denoted as $\phi^{(N)}$ (Fig. 3).

The experimentally measured $g^{(3)}$ function (Fig. 2A, B) displays a clear bunching feature: the probability to detect three photons within a short time ($\lesssim 25$ ns) of one another is six times larger than for non-interacting photons in a laser beam. The increase at $t_1 = t_2 = t_3$ is accompanied by a depletion region for photons arriving within $\sim 0.7 \mu s$

of one another, particularly visible along the lines of two-photon correlations $t_i = t_j \neq t_k$ (Fig. 2A): This depletion region is caused by the inflow of probability current towards the center $t_1 = t_2 = t_3$. Figure 2B compares the two-photon correlation function $g^{(2)}(t, t + |\tau|)$ to that for three photons of which two photons were detected in the same time bin, $g^{(3)}(t, t, t + |\tau|)$. The trimer feature is approximately a factor of 2 narrower than the dimer feature, showing that a photon is attracted more strongly to two other photons than to one. Figure 2C illustrates the binding of a third photon to two photons that are detected with a time separation T . If T exceeds the dimer time scale τ_2 , then the third photon binds independently to either photon, while for $T < \tau_2$ the two peaks merge into a single, more tightly bound trimer. This is analogous to the binding of a particle to a double-well potential as the distance between the wells is varied, since the polaritons can be approximately described as interacting massive particles moving at finite group velocity (6).

The dispersive and distance-dependent photon-photon interaction also manifests itself in a large conditional phase shift that depends on the time interval τ between the detection of the conditioning photons (at times $t_1 = t_2 = t$) and the phase measurement on detector D_3 at time t_3 . We observe a conditional phase shift $\phi^{(3)}(t, t, t + |\tau|)$ for the trimer near $\tau = 0$ (Fig. 3A) that is significantly larger than the dimer phase shift $\phi^{(2)}(t, t + |\tau|)$ (Fig. 3B). This confirms the stronger interaction between a photon and a dimer compared to that between one photon and another.

To understand these results quantitatively, we apply an effective field theory (EFT) (21) which describes the low-energy scattering of Rydberg polaritons. This EFT gives us a one-dimensional slow-light Hamiltonian density with a contact interaction.

$$\mathcal{H} = -\hat{\psi}^\dagger \left(i\hbar v_g \partial_z + \frac{\hbar^2}{2m} \partial_z^2 \right) \hat{\psi} - \frac{\hbar^2}{ma} \hat{\psi}^{\dagger 2} \hat{\psi}^2, \quad (2)$$

where v_g is the group velocity inside the medium, $m = -\hbar\Omega_c^2/(8\Delta v_g^2)$ is the effective photon mass, a is the scattering length, Ω_c is the control laser Rabi frequency, and Δ is the one-photon detuning. For weak interactions, $a \approx 15.28(\frac{1}{\text{OD}_B} \frac{\Delta}{\Gamma})^2 r_B$ (21, 22). The contact model provides an accurate description of the low-energy scattering whenever $a \gg r_B$, the microscopic range of the two-body potential. For our parameters, we find this is well satisfied as $a \gtrsim 10r_B$. $\hat{\psi}$ is a quantum field annihilation operator, which corresponds to a photon outside the medium and a Rydberg polariton inside. Note that for our blue-detuned probe, the effective mass is negative and the interaction is repulsive. This situation maps onto a system with a positive mass and attractive interaction. The transverse mass is substantially heavier than m (23), effectively freezing out the transverse degrees of freedom over the timescale of the experiment. The bound states can be determined from the exact solution of this model for finite particle numbers (24, 25), resulting in the correlation functions $g^{(3)}(t_1, t_2, t_3) \propto e^{-\frac{|t_1-t_2|}{a/(2v_g)}} e^{-\frac{|t_2-t_3|}{a/(2v_g)}} e^{-\frac{|t_1-t_3|}{a/(2v_g)}}$ and $g^{(2)}(t_1, t_2) \propto e^{-\frac{|t_1-t_2|}{a/(2v_g)}}$.

In the case $t_1 = t_2 = t$, we find that $g^{(3)}(t, t, t + |\tau|) \propto e^{-2\frac{|\tau|}{a/(2v_g)}}$, implying that the width of three-photon wave-packet (corresponding to $g^{(3)}$) is half that of $g^{(2)}$ for the same experimental conditions, in good agreement with experimental observations. We calculate $a/(2v_g) = 0.32 \mu\text{s}$ for our measured experimental parameters (26) and find it to be consistent with data (Fig. 2B, dashed lines). Following the quantum quench at the entry of the medium, the initial state is decomposed into the bound state and the continuum of scattering states (6). Near $\tau = 0$, the scattering states dephase with each other, while the bound state propagates without distortion (26). This leads to a small contribution of scattering states in this region, with the bound state dominating the $g^{(3)}$ function. The observed value of $g^{(3)}(0)$ is not universal, as it is affected by the contributions from long-wavelength scattering states and nonlinear losses in the system and, therefore, depends on the atomic density profile of the medium. The dimer and trimer binding energies

can be estimated as $E_2 = -\frac{\hbar^2}{ma^2} = \hbar \times 0.2$ MHz and $E_3 = 4E_2$ respectively. This binding energy is $\sim 10^{10}$ times smaller than in diatomic molecules such as NaCl and H_2 , but is comparable to Feshbach (27) and Efimov (28) bound states of atoms with similar mass m and scattering length a . To further characterize the three-photon bound state, it is instructive to consider the phase ratio $\phi^{(3)}/\phi^{(2)}$. For the bound-state contribution to the conditional phase $\phi^{(3)}(t, t, t)$ ($\phi^{(2)}(t, t)$), the Hamiltonian of Eq.2 predicts a phase that equals the trimer binding energy times the propagation time in the medium. Thus from the bound state contributions, one would expect a ratio $\phi^{(3)}/\phi^{(2)} = 4$, independent of the atom-light detuning Δ . While the observed ratio (Fig. 4B) is approximately constant, it is smaller than 4.

The observed deviation is likely due to the two contributions of comparable magnitude. One correction arises from the scattering states, or equivalently, from the fact that our Rydberg medium (~ 130 μm) is comparable in size to the two-photon bound state (~ 280 μm). For a medium that is short compared to the bound state, one expects the ratio to be 3, consistent with a dispersionless Kerr medium (29). The other, more fundamental correction, may be due to a contribution that does not arise from pairwise interactions, effectively representing a three-photon force. Specifically, when all three photons are within one blockade radius of one another, there can be only one Rydberg excitation and the potential cannot exceed the value corresponding to that of two photons (21, 30). This saturation effect manifests itself as a short-range repulsive effective three-photon force which, according to our theoretical analysis (26), results in a reduction of $\phi^{(3)}/\phi^{(2)}$ below 3. The corresponding correction to the bound state is smaller in the weakly interacting regime relevant to these experiments (30). This explains why the effective three-photon force has a relatively weak effect on the bunching of $g^{(3)}(|\tau| < 0.2$ μs), which is dominated by the bound state. Note that both the scaling arguments and numerical evidence indicate

that the effective three-photon force contributes to the three-body scattering amplitudes more strongly than two-body finite range effects in this regime (21).

To quantitatively understand these effects, the EFT is modified to include the estimated effective three-photon force (26). Using the modified EFT, we compare the results with and without the repulsive effective three-photon force, while also taking into account the effects due to finite medium (Fig. 4B). Including this three-photon saturation force allows the phase ratio $\phi^{(3)}/\phi^{(2)}$ to go below 3, in a reasonable agreement with the experimental observations. For fully saturated interactions between the polaritons, the interaction potential does not increase with photon number, and the phase ratio should approach 2.

The observation of the three-photon bound state, which can be viewed as photonic solitons in the quantum regime (7, 8), can be extended along several different directions. First, increasing the length of the medium at constant atomic density would remove the effect of the scattering states through destructive quantum interference to larger τ and retain only the solitonic bound-state component. Additionally, the strong observed rate dependence of $\phi^{(3)}$ may indicate that larger photonic molecules and photonic clusters could be observed with improved detection efficiency and data acquisition rate. Furthermore, using an elliptical or larger round probe beam and carefully engineering the mass along different directions, the system can be extended to two and three dimensions, possibly permitting the observation of photonic Efimov states (31, 32). Finally, our medium only supports one two/three-photon bound state, corresponding to a nonlinear phase less than π . A threefold increase in the atomic density would render the interaction potential sufficiently deep for a second bound state to appear near zero energy, which should result in resonant photon-photon scattering and a tunable scattering length (22). The presence of large effective N-body forces in this system opens intriguing possibilities to study

exotic many-body phases of light and matter, including self-organization in open quantum systems (33, 34), and quantum materials that cannot be realized with conventional systems.

Acknowledgments: We thank O. Firstenberg for early stages of this work and S. Choi for discussions. MJG and AVG thank H. P. Büchler for many insightful discussions and comments on the theoretical analysis. This work has been supported by NSF, NSF CUA, ARO, AFOSR, ARO MURI and Bush Fellowship. AVG and MJG acknowledge support by ARL CDQI, NSF QIS, and NSF PFC at JQI. CC acknowledges funding support from NSF grant PHY-1511696 and Alexander von Humboldt foundation. Data are available upon request.

Supplementary Materials

Materials and Methods

Supplementary Text

Figs. S1 to S4

Tables S1 to S2

References (*35-40*)

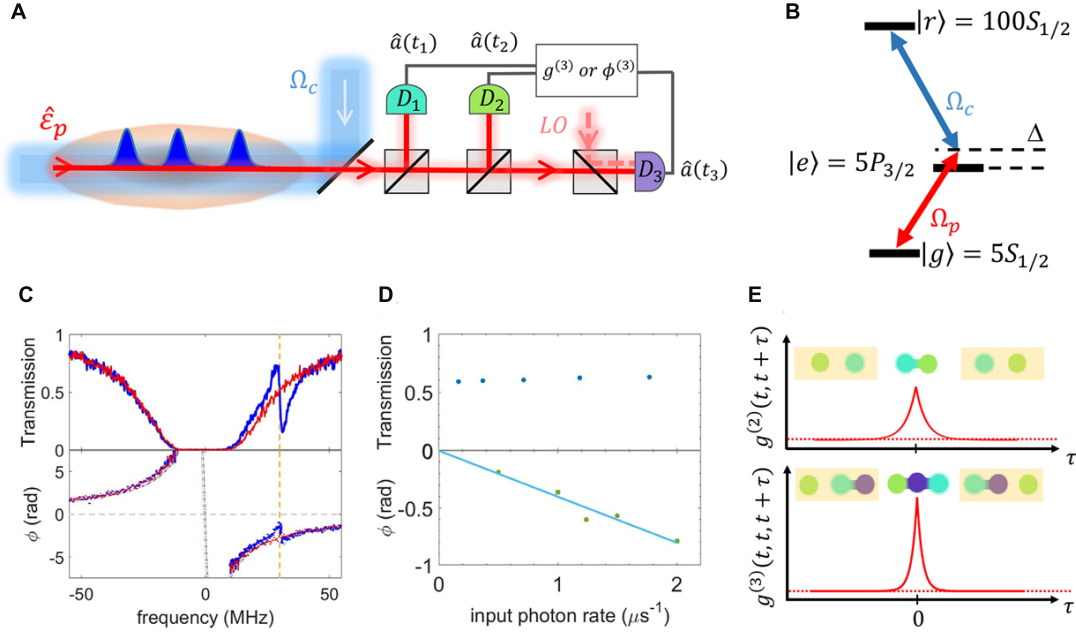


Figure 1: **Qualitative descriptions of the experiment.** **A,B,** Setup and atomic level scheme. The atoms are optically pumped into the hyperfine (F) and magnetic (m_F) sublevel $|g\rangle = |5S_{1/2}, F = 2, m_F = 2\rangle$. The weak coherent probe light is coupled to the Rydberg state $|r\rangle = |100S_{1/2}, m_J = 1/2\rangle$, via an intermediate state $|e\rangle = |5P_{3/2}, F = 3, m_F = 3\rangle$, with linewidth $\Gamma/2\pi = 6.1$ MHz, by means of a counter-propagating control field that is detuned by Δ below the resonance frequency of the upper transition, $|e\rangle \rightarrow |r\rangle$. Strong interactions between probe photons are detected via photon correlations of the transmitted light, which is split onto three single-photon detectors with equal intensities. To perform phase measurements, a local oscillator is mixed into detector D_3 . **C,** Transmission (top) and phase ϕ (bottom) as a function of probe frequency measured at a low ($0.5 \mu\text{s}^{-1}$) input photon rate. ϕ is measured without conditioning on the detection of other photons. The control laser is set at $\Delta/2\pi = 30$ MHz below the $|e\rangle \rightarrow |r\rangle$ transition with Rabi frequency $\Omega_c/2\pi = 10$ MHz. The blue and red data are from measurements with and without control beam, respectively. The blue and red dashed lines in the bottom graph are theoretical expectations. The vertical yellow dashed line marks EIT resonance. **D,** Rate dependence of transmission (top) and unconditional phase (bottom) on two-photon resonance $|g\rangle \rightarrow |r\rangle$, with a one-photon detuning of $\Delta/2\pi = 30$ MHz, and control Rabi frequency $\Omega_c/2\pi = 10$ MHz. While the transmission is rate-independent, the phase is strongly rate dependent (slope is $0.4 \text{ rad} \cdot \mu\text{s}$). **E.** Schematic correlation functions for two (top) and three (bottom) photons as a function of their time separation τ . The attractive interaction leads to photon bunching, with three photons being more tightly bound together than two photons.

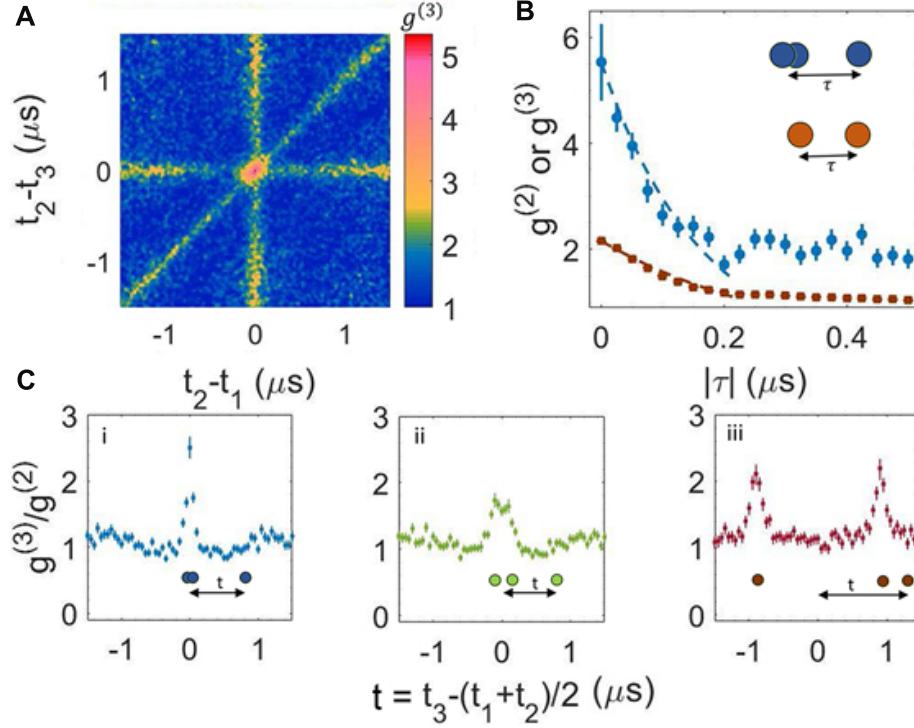


Figure 2: Photon correlation functions with tighter bunching due to the three-photon bound state. Photon correlation functions measured at one-photon detuning $\Delta/2\pi = 30$ MHz, control Rabi frequency $\Omega_c/2\pi = 10$ MHz, input photon rate of $1 \mu\text{s}^{-1}$ and on EIT resonance. **A**, Two-dimensional representation of three-photon correlation function $g^{(3)}(t_1, t_2, t_3)$, with t_i being the photon detection time at detector D_i . Three-photon bunching corresponds to the central region, two-photon bunching to the stripes. **B**, $g^{(3)}(t, t, t + |\tau|)$ (blue data points) and $g^{(2)}(t, t + |\tau|)$ (brown data points), with the decay constants calculated from the exact solution for the bound states $\tau_3^c = 0.16 \mu\text{s}$ and $\tau_2^c = 0.32 \mu\text{s}$ respectively (dashed lines). The calculated exponential decay is scaled to match the initial point of the measured intensity correlation functions. The approximately twice smaller decay length of the three-photon correlation function shows that a photon is more strongly bound to two photons than to one. The fitted exponential decay constants with zero offset for $g^{(3)}$ and $g^{(2)}$ are $\tau_3 = 0.14(2) \mu\text{s}$ and $\tau_2 = 0.31(6) \mu\text{s}$, respectively (not shown), in agreement with the calculated values. **C**, Three representative plots of $g^{(3)}(t_1, t_2, t_3)/g^{(2)}(t_1, t_2)$ for fixed $T \equiv |t_1 - t_2| = 0 \mu\text{s}$ (i), $T = 0.2 \mu\text{s}$ (ii), and $T = 1.8 \mu\text{s}$ (iii), within a 50 ns window. As we condition on the two photons being further and further away, the sharply decaying $g^{(3)}$ function transitions to a slower decaying $g^{(2)}$ function. For intermediate time separations (ii), there is interference between all states including the dimer and trimer. All permutations of the detectors are used to generate the data in B,C. Error bars in figure indicate one standard deviation (s.d). Error bars in the fitted exponential decay constants indicate one s.d of the fit.

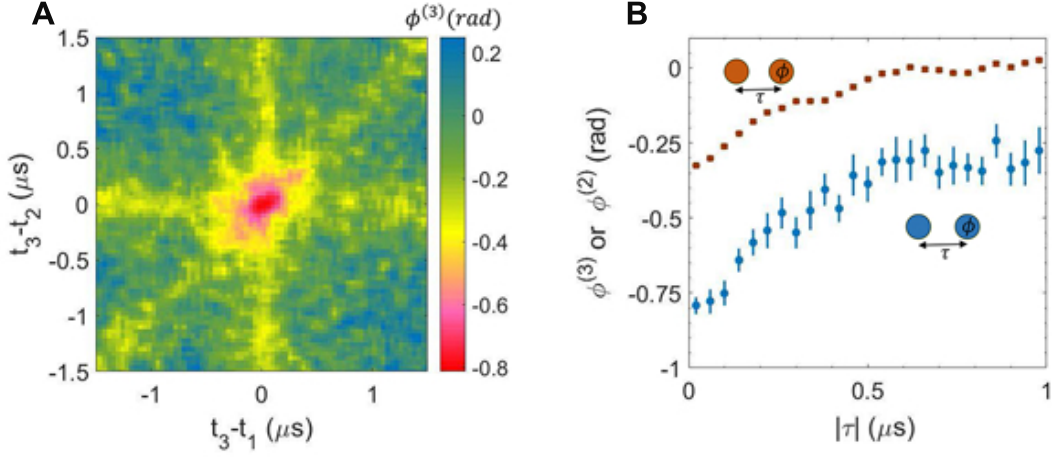


Figure 3: Larger nonlinear phase for three photons. Nonlinear phase measured under identical conditions as the data in Fig. 2. **A**, Conditional phase $\phi^{(3)}(t_1, t_2, t_3)$, where t_1 and t_2 correspond to photon detection events at detectors D_1 , D_2 , and a heterodyne measurement is performed on detector D_3 at time t_3 . **B**, Diagonal cut $\phi^{(3)}(t, t, t + |\tau|)$ (blue), with the two conditioning probe photons within 40 ns of each other, and $\phi^{(2)}(t, t + |\tau|)$ (brown), showing a larger phase when conditioning on two other near-simultaneous photons ($\phi^{(3)}$) than on one near-simultaneous photon ($\phi^{(2)}$). $\phi^{(N)}$ is referenced to its own average value when all the N photons are too far apart from each other to be correlated. Specifically, $\phi^{(2)}(t_1, t_2) \equiv \tilde{\phi}^{(2)}(t_1, t_2) - (\tilde{\phi}^{(1)}(t_1) + \tilde{\phi}^{(1)}(t_2)) \xrightarrow{|t_1 - t_2| \rightarrow \infty} 0$, and $\phi^{(3)}(t_1, t_2, t_3) \equiv \tilde{\phi}^{(3)}(t_1, t_2, t_3) - (\tilde{\phi}^{(1)}(t_1) + \tilde{\phi}^{(1)}(t_2) + \tilde{\phi}^{(1)}(t_3)) \xrightarrow{|t_i - t_j| \rightarrow \infty, \forall i \neq j} 0$. $\phi^{(3)}$ at large $|\tau|$ asymptotically goes to $\phi^{(2)}(t, t)$, because $\phi^{(3)}(t, t, t + |\tau|) \xrightarrow{|\tau| \rightarrow \infty} \tilde{\phi}^{(2)}(t, t) + \tilde{\phi}^{(1)}(t + |\tau|) - (\tilde{\phi}^{(1)}(t) + \tilde{\phi}^{(1)}(t) + \tilde{\phi}^{(1)}(t + |\tau|)) = \phi^{(2)}(t, t)$. Error bars indicate one s.d.

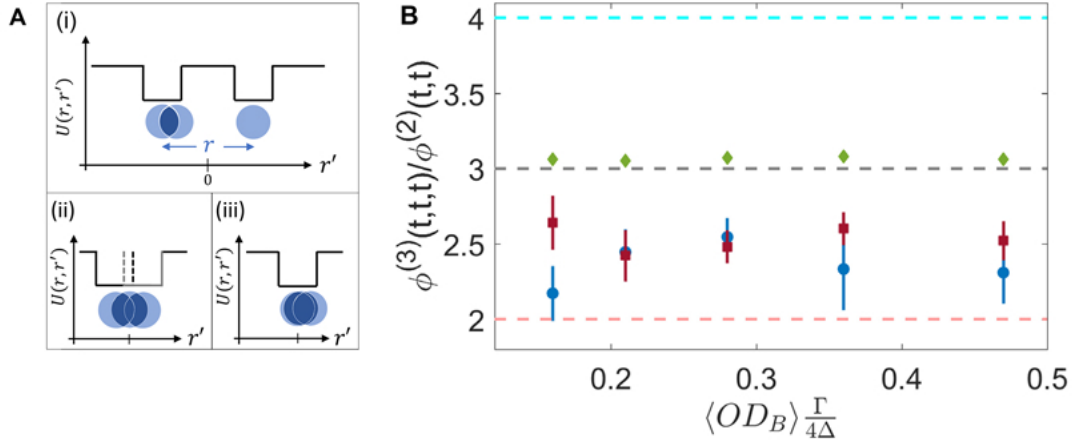


Figure 4: **Comparison of the phase ratio with the EFT predictions.** **A** illustrates the potential (solid black and gray lines) the third photon, at position r' , experiences due to the other two photons, at positions $\pm r/2$. (i) When the two photons are separated by more than twice the blockade radius ($r > 2r_B$), each of them creates its own square potential with a width of $2r_B$; (ii) When the two photons overlap ($r_B < r < 2r_B$), the potential is partially saturated; (iii) When the two photons are within one blockade radius ($r < r_B$), since there can be at most one Rydberg excitation within r_B , the potential is not deeper than that created by one photon. Therefore, we overestimate the attractive potential by considering pairwise interaction only, and a repulsive effective three-photon force is required to correctly take into account the saturation of the Rydberg blockade. **B**, Measured phase ratio $\phi^{(3)}(t, t, t)/\phi^{(2)}(t, t)$ (blue) and the EFT predictions (with the effective three-photon force in brown; without in green) as a function of $\langle OD_B \rangle \frac{\Gamma}{4\Delta}$, where $\langle \rangle$ refers to the average over the Gaussian profile of the atomic density. The quantity $\langle OD_B \rangle \frac{\Gamma}{4\Delta}$ is a quantitative measure of the interaction strength in this system. The control Rabi frequency $\Omega_c/2\pi = \{22, 18, 10, 10, 8\}$ MHz for $\Delta/2\pi = \{54, 42, 30, 24, 18\}$ MHz is chosen such that the transmission is insensitive to the input photon rate (Fig. 1C). We also change the input photon rate $\{0.7, 1, 1, 1.3, 2.5\}$ photons/ μ s to achieve similar data acquisition rates since the losses are larger at smaller detunings. For a fully saturated medium, one expects $\phi^{(3)}/\phi^{(2)} = 2$, as indicated by the pink dashed line; for bound states in a long medium and no effective three-photon force, one expects $\phi^{(3)}/\phi^{(2)} = 4$, as indicated by the cyan dashed line (see text). EFT results are calculated with parameters from independent measurements, and the two-photon detuning from the EIT resonance is the only parameter varied within the experimental uncertainty to fit the two-photon phase. Error bars in the EFT with the effective three-photon force arise from the variations with the choice of matching conditions for the three-body scattering amplitudes (26). Error bars in the experimental data indicate one s.d.

References and Notes

1. I. H. Deutsch, R. Y. Chiao, J. C. Garrison, Diphotons in a nonlinear fabry-pérot resonator: bound states of interacting photons in an optical “quantum wire”, *Phys. Rev. Lett.* **69**, 3627 (1992).
2. J.-T. Shen, S. Fan, Strongly correlated two-photon transport in a one-dimensional waveguide coupled to a two-level system, *Phys. Rev. Lett.* **98**, 153003 (2007).
3. P. Drummond, H. He, Optical mesons, *Phys. Rev. A* **56**, R1107 (1997).
4. Z. Cheng, G. Kurizki, Optical “multiexcitons”: quantum gap solitons in nonlinear bragg reflectors, *Phys. Rev. Lett.* **75**, 3430 (1995).
5. Y. Shen, J.-T. Shen, Photonic-fock-state scattering in a waveguide-qed system and their correlation functions, *Phys. Rev. A* **92**, 033803 (2015).
6. O. Firstenberg, *et al.*, Attractive photons in a quantum nonlinear medium, *Nature* **502**, 71 (2013).
7. P. D. Drummond, R. M. Shelby, S. R. Friberg, Y. Yamamoto, Quantum solitons in optical fibres, *Nature* **365**, 307 (1993).
8. Y. Lai, H. Haus, Quantum theory of solitons in optical fibers. ii. exact solution, *Phys. Rev. A* **40**, 854 (1989).
9. D. Chang, *et al.*, Crystallization of strongly interacting photons in a nonlinear optical fibre, *Nature Phys.* **4**, 884 (2008).
10. M. F. Maghrebi, *et al.*, Fractional quantum hall states of rydberg polaritons, *Phys. Rev. A* **91**, 033838 (2015).

11. L. Li, A. Kuzmich, Quantum memory with strong and controllable rydberg-level interactions, *Nature Comm.* **7** (2016).
12. J.-W. Pan, *et al.*, Multiphoton entanglement and interferometry, *Rev. Mod. Phys.* **84**, 777 (2012).
13. I. Friedler, D. Petrosyan, M. Fleischhauer, G. Kurizki, Long-range interactions and entanglement of slow single-photon pulses, *Phys. Rev. A* **72**, 043803 (2005).
14. D. Petrosyan, J. Otterbach, M. Fleischhauer, Electromagnetically induced transparency with rydberg atoms, *Phys. Rev. Lett.* **107**, 213601 (2011).
15. A. V. Gorshkov, J. Otterbach, M. Fleischhauer, T. Pohl, M. D. Lukin, Photon-photon interactions via rydberg blockade, *Phys. Rev. Lett.* **107**, 133602 (2011).
16. H. Labuhn, *et al.*, Tunable two-dimensional arrays of single rydberg atoms for realizing quantum ising models, *Nature* **534**, 667 (2016).
17. Y. Dudin, A. Kuzmich, Strongly interacting rydberg excitations of a cold atomic gas, *Science* **336**, 887 (2012).
18. T. Peyronel, *et al.*, Quantum nonlinear optics with single photons enabled by strongly interacting atoms, *Nature* **488**, 57 (2012).
19. D. Maxwell, *et al.*, Storage and control of optical photons using rydberg polaritons, *Phys. Rev. Lett.* **110**, 103001 (2013).
20. J. D. Thompson, *et al.*, Symmetry-protected collisions between strongly interacting photons, *Nature* **542**, 206 (2017).

21. M. J. Gullans, *et al.*, Effective field theory for rydberg polaritons, *Phys. Rev. Lett.* **117**, 113601 (2016).
22. P. Bienias, *et al.*, Scattering resonances and bound states for strongly interacting Rydberg polaritons, *Phys. Rev. A* **90**, 53804 (2014).
23. M. Fleischhauer, J. Otterbach, R. G. Unanyan, Bose-einstein condensation of stationary-light polaritons, *Phys. Rev. Lett.* **101**, 163601 (2008).
24. E. H. Lieb, W. Liniger, Exact analysis of an interacting bose gas. i. the general solution and the ground state, *Phys. Rev.* **130**, 1605 (1963).
25. J. B. McGuire, Study of exactly soluble one-dimensional n-body problems, *Journal of Mathematical Physics* **5**, 622 (1964).
26. Supplementary information is available at the Science Web site.
27. C. Chin, R. Grimm, P. Julienne, E. Tiesinga, Feshbach resonances in ultracold gases, *Rev. Mod. Phys.* **82**, 1225 (2010).
28. E. Braaten, H.-W. Hammer, Efimov physics in cold atoms, *Annals of Physics* **322**, 120 (2007).
29. P. Bienias, H. P. Büchler, Quantum theory of kerr nonlinearity with rydberg slow light polaritons, *New Journal of Physics* **18**, 123026 (2016).
30. K. Jachymski, P. Bienias, H. P. Büchler, Three-body interaction of rydberg slow-light polaritons, *Phys. Rev. Lett.* **117**, 053601 (2016).
31. M. Gullans, *et al.*, Efimov states of strongly interacting photons, *arXiv preprint arXiv:1709.01955* (2017).

- 32. T. Kraemer, *et al.*, Evidence for efimov quantum states in an ultracold gas of caesium atoms, *Nature* **440**, 315 (2006).
- 33. N. Thaicharoen, A. Schwarzkopf, G. Raithel, Control of spatial correlations between rydberg excitations using rotary echo, *Phys. Rev. Lett.* **118**, 133401 (2017).
- 34. P. Schausz, *et al.*, Observation of spatially ordered structures in a two-dimensional rydberg gas, *Nature* **491**, 87 (2012).
- 35. H. Carmichael, R. Brecha, P. Rice, Quantum interference and collapse of the wavefunction in cavity qed, *Optics communications* **82**, 73 (1991).
- 36. S. K. Adhikari, T. Frederico, I. Goldman, Perturbative renormalization in quantum few-body problems, *Phys. Rev. Lett.* **74**, 487 (1995).
- 37. E. Braaten, H.-W. Hammer, Universality in few-body systems with large scattering length, *Physics Reports* **428**, 259 (2006).
- 38. P. F. Bedaque, H.-W. Hammer, U. Van Kolck, Renormalization of the three-body system with short-range interactions, *Phys. Rev. Lett.* **82**, 463 (1999).
- 39. P.-É. Larré, I. Carusotto, Propagation of a quantum fluid of light in a cavityless nonlinear optical medium: General theory and response to quantum quenches, *Phys. Rev. A* **92**, 043802 (2015).
- 40. M. J. Gullans, Controlling atomic, solid-state and hybrid systems for quantum information processing, Ph.D. thesis, Harvard University (2013).

Contents

S1. Materials and Methods	1
A. Atom loading and preparation	1
B. Correlation and phase measurement setup	2
C. <i>Ab initio</i> calculation of the initial slope of the correlation functions	3
S2. Supplementary Text	3
A. Microscopic Model	3
B. Effective Field Theory	5
1. Estimating the Three-Body Force	5
2. Comparison Between EFT, Numerical Simulations, and Experimental Data	7
C. Formation of N -Body Bound States	8
D. Finite Rate Corrections to Theory	9
E. Dissipative Corrections to Theory	11
Supplementary References	12

S1. MATERIALS AND METHODS

A. Atom loading and preparation

The ^{87}Rb atoms are loaded from a 3D magneto-optical trap (MOT) into a 1064 nm crossed dipole trap. The dipole trap is modulated with a period of 40 μs and 80 % duty cycle. A $\sim 6 \mu\text{s}$ long probe pulse is sent to the atomic cloud while the dipole trap is off to avoid inhomogeneous AC Stark shift and the anti-trapping of the Rydberg atoms. The modulation of the trap and therefore the measurements last for 120 ms before a new atomic cloud is loaded. The average resonant optical depth along the atomic cloud is 36. The root-mean-square (RMS) length of the medium is $\sigma_{\text{ax}} = 32 \mu\text{m}$. The atoms are optically pumped into the hyperfine (F) and magnetic (m_F) sublevel $|g\rangle = |5S_{1/2}, F = 2, m_F = 2\rangle$. The weak coherent probe light is coupled to the Rydberg state, via an intermediate state $|e\rangle = |5P_{3/2}, F = 3, m_F = 3\rangle$, of linewidth $\Gamma/2\pi = 6.1$ MHz, by means of a counter-propagating control field that is detuned by Δ below the resonance frequency of the upper transition, $|e\rangle \rightarrow |r\rangle = |100S_{1/2}, m_J = 1/2\rangle$, in the presence of a 3 G magnetic field along the long axis of the cloud. Probe and control counter-propagate along the quantization axis. The blockade radius r_B defined as $\left(C_6 \frac{2|\Delta|}{\Omega_c^2}\right)^{\frac{1}{6}}$ is 20 μm , where $C_6/\hbar = 2\pi \times 56.4 \text{ THz} \cdot (\mu\text{m}^6)$ is the van der Waals coefficient and $\Delta = 30 \text{ MHz}$ is the one-photon detuning.

B. Correlation and phase measurement setup

In Fig. 1A of the main text, the first two beamsplitters are polarizing beamsplitters (PBS), and the last one is a 8:92 pellicle beamsplitter to minimize loss of the probe photons. There are polarization optics (not shown in the figure) before the first PBS to clean up the polarization of the probe, after which a half-wave plate is placed before each PBS to balance the detection rates on the three detectors.

We obtain the phase by performing a heterodyne measurement by mixing the transmitted probe light with a local oscillator (LO) at detector D_3 as shown in Fig. 1A. The LO is blue detuned by 79 MHz from the probe laser and this frequency difference is generated by an acousto-optic modulator (AOM). Afterwards, the two beams are sent through their own optical fibers. In order to take out the phase fluctuations caused by the fibers, we interfere the probe and LO, and trigger the single-photon detectors with the beatnote, which serves as a time zero for each probe pulse. Unlike the probe, the LO does not propagate through the atomic cloud, causing an additional phase drift on a time scale of tens of milliseconds. We keep track of the overall phase drift by fitting the unconditional phase for each time interval of ~ 10 ms. The interpolation of this time-dependent unconditional phase is added to each detection event on detector D_3 (phase measurement) to enable averaging over hours for the conditional phase measurements. Since we only detect one output port of the pellicle beamsplitter, the intensity noise cannot be canceled as in a balanced detection. Therefore, the LO counts is kept about four times of that of the probe on detector D_3 .

To produce the unconditional phase measurement in Fig. 1C of the main text, we modulate probe-dipole trap for 5 ms. The sequence is adjusted such that during this 5 ms measurement time, the average optical depth is the same as a usual sequence. After that, we shut off the dipole trap and allow the atomic cloud to expand for 1 ms. We then measure the unconditional phase for 4 ms and use it as the phase reference.

The rate-dependent $\phi^{(1)}$ in Fig. 1D of the main text is generated by alternating relatively strong and weak (input photon rate of $0.5 \mu\text{s}^{-1}$) pulses. The weak pulse serves as the phase reference, and a constant offset is applied to all the points such that the linear fit crosses the origin.

By conditioning on detecting two probe photons at time t_1 and t_2 , and performing a phase measurement at time t_3 , we directly measure $\tilde{\phi}^{(3)}(t_1, t_2, t_3) - \tilde{\phi}^{(2)}(t_1, t_2) - \tilde{\phi}_{ref}^{(3)}$. From the same data, by conditioning on detecting one probe photon, we obtain $\tilde{\phi}^{(2)}(t_1, t_2) - \tilde{\phi}^{(1)}(t_1) - \tilde{\phi}_{ref}^{(2)}$, where $\tilde{\phi}_{ref}^{(N)}$ denotes the phase reference of the directly measured phase conditioning on detecting $N-1$ probe photons. We can use the local unconditional phase when the phase measurement is performed as the reference, as in Fig. S1, namely, $\tilde{\phi}_{ref}^{(3)} = \tilde{\phi}^{(1)}(t_3)$ and $\tilde{\phi}_{ref}^{(2)} = \tilde{\phi}^{(1)}(t_2)$. For uncorrelated photons, N -photon phase can be written as the sum of the one-photon phase, e.g. $\tilde{\phi}^{(3)}(t_1, t_2, t_3) \xrightarrow{|t_i - t_j| \rightarrow \infty, \forall i \neq j} \tilde{\phi}^{(1)}(t_1) + \tilde{\phi}^{(1)}(t_2) + \tilde{\phi}^{(1)}(t_3)$. Therefore, at large $|\tau|$, both conditional phases in Fig. S1 are expected to go to 0. However, there is small disagreement

between the unconditional and the conditional phase with well separated photons. The conditional phases vary at a time scale of a few tens of microseconds, much slower than the bound state physics. Additionally, the mismatch is only less than 20 % of the phase of the concurrent photons. Therefore, we do not believe the phase offset at large τ to have significant impact on our main results.

In the main text, on the other hand, we use its own average value when the two photons are far away from each other as the phase reference $\tilde{\phi}_{ref}^{(2)}, \tilde{\phi}_{ref}^{(3)}$ includes both the phase of the uncorrelated photons and the phase conditioning on detecting one probe photon, namely, $\tilde{\phi}_{ref}^{(3)} = \tilde{\phi}^{(1)}(t_3) - (\tilde{\phi}^{(2)}(t_1, t_2) - \tilde{\phi}^{(1)}(t_1) - \tilde{\phi}_{ref}^{(2)})$. Assuming all detectors are interchangeable, this leads to $\tilde{\phi}^{(3)}(t_1, t_2, t_3) - (\tilde{\phi}^{(1)}(t_1) + \tilde{\phi}^{(1)}(t_2) + \tilde{\phi}^{(1)}(t_3))$, defined as $\phi^{(3)}(t_1, t_2, t_3)$ in the main text.

C. *Ab initio* calculation of the initial slope of the correlation functions

We independently measure OD, the control Rabi frequency Ω_c , the one-photon detuning Δ , the root-mean-square length of the medium σ_{ax} and the group delay (the propagation time of the photon in the medium). The blockade radius r_B is calculated from the measured Ω_c , Δ and the known C_6 coefficient. The optical depth per blockade radius OD_B is calculated from the measured OD and RMS length of the cloud σ_{ax} assuming a Gaussian atomic density profile. The population decay rate Γ is taken from the known natural linewidth. The group velocity v_g is calculated from the measured group delay and σ_{ax} . We then use these quantities to calculate the scattering length and $\tau_{2,3}$.

S2. SUPPLEMENTARY TEXT

A. Microscopic Model

These experiments can be understood schematically in terms of the multi-particle transport problem illustrated in Fig. S2. A coherent state of light is incident on the quantum nonlinear optical medium formed from Rydberg atoms. Due to the interactions inside the medium, the output light exhibits multi-photon entanglement and correlations. Developing a full theoretical description of the transmitted light field is challenging even in the limit of a few-photons because the photons must be treated as a continuous quantum field. Nevertheless significant simplifications in the theory are possible due to the large separation of scales between the microscopic degrees of freedom and the emergent scales present in the correlations of the output light. We recently developed an effective field theory (EFT) description of this transmission problem by taking advantage of this large separation of scales [S1]. This EFT framework forms the basis of our theoretical analysis of the three-photon transmission problem studied in this work.

As the starting point for our theory we use a continuum description of the problem which first coarse grains over the atomic density to define local continuous quantum fields $\psi_g(z)$, $\psi_p(z)$, and

$\psi_s(z)$ for the photons, intermediate atomic excited state, and Rydberg state, respectively. These operators satisfy bosonic commutation relations $[\psi_a(z), \psi_b^\dagger(z')] = \delta_{ab}\delta(z-z')$. In describing the transmission of the photonic field ψ_g , we integrate out the other transverse propagating photonic degrees of freedom to arrive at a master equation description of the problem ($\hbar = 1$)

$$\dot{\rho} = -i \int dz [\mathcal{H}_0(z) + \mathcal{H}_{\text{int}}(z), \rho] + \frac{\Gamma}{2} \int dz \mathcal{D}[\psi_p(z)]\rho + \frac{\gamma_s}{2} \int dz \mathcal{D}[\psi_s(z)]\rho, \quad (\text{S1})$$

$$\mathcal{H}_0(z) = \begin{pmatrix} \psi_g(z) \\ \psi_p(z) \\ \psi_s(z) \end{pmatrix}^\dagger \begin{pmatrix} -ic\partial_z & g(z) & 0 \\ g(z) & -\Delta & \Omega_c/2 \\ 0 & \Omega_c/2 & -\delta \end{pmatrix} \begin{pmatrix} \psi_g(z) \\ \psi_p(z) \\ \psi_s(z) \end{pmatrix}, \quad (\text{S2})$$

$$\mathcal{H}_{\text{int}} = \int dz' \psi_s^\dagger(z) \psi_s^\dagger(z') V(z-z') \psi_s(z') \psi_s(z), \quad (\text{S3})$$

where $\mathcal{D}[A]\rho = -\{A^\dagger A, \rho\} + 2A\rho A^\dagger$ is a trace-perserving superoperator, \mathcal{H}_0 is the non-interacting Hamiltonian density written in the rotating frame, and \mathcal{H}_{int} is the Rydberg interaction Hamiltonian density. The non-interacting theory is parameterized in terms of the control field Rabi frequency Ω_c , the fullwidth of the intermediate state Γ , the fullwidth of the Rydberg state γ_s , the detuning $\Delta = \omega_{ps} - \omega_c$ between the control field frequency ω_c and the Rydberg-intermediate state transition frequency ω_{ps} , and the two-photon detuning $\delta = \omega_p + \omega_c - \omega_{gs}$ between the sum of ω_c and the input probe frequency ω_p and the ground to Rydberg state transition frequency ω_{gs} . The single-photon Rabi frequency for the probe $g(z)$ is proportional to the square root of the atomic density $n(z)$, with the proportionality constant determined by the resonant optical depth $\text{OD} = \int dz 4[g(z)]^2/\Gamma c$. We parameterize the density by a Gaussian profile $n(z) \propto \exp(-z^2/2\sigma_{\text{ax}}^2)$, where σ_{ax} is the RMS axial width of the cloud. Finally, we approximate the Rydberg interactions by their long-range van der Waals tail $V(r) = C_6/r^6$.

An important simplification of this problem is provided for photonic input states with a low photon rate, where the evolution can be described solely in terms of the dynamics induced by the effective non-Hermitian Hamiltonian [S2]

$$\mathcal{H}_{\text{eff}} = \mathcal{H}_0 + \mathcal{H}_{\text{int}} - i\frac{\Gamma}{2}\psi_p^\dagger\psi_p - i\frac{\gamma_s}{2}\psi_s^\dagger\psi_s. \quad (\text{S4})$$

The decay terms can be incorporated into \mathcal{H}_0 through the replacements $\Delta \rightarrow \Delta + i\Gamma/2$ and $\delta \rightarrow \delta + i\gamma_s/2$. This approximation relies on the fact that the corrections to the non-Hermitian Hamiltonian evolution from the recycling terms in the master equation, i.e., the so-called “quantum jumps,” are suppressed by higher powers of the polariton density in the medium (see Ref. [S3] for a similar argument applied to a cavity model). Since the experiments are operated in the limit of low polariton densities in the medium, we are justified in neglecting these quantum jump processes. We present a more detailed discussion of these effects in Sec. S2 E.

B. Effective Field Theory

For sufficiently low-energy scattering of two-particles, the dynamics of the Rydberg polaritons are described by the renormalized Lagrangian density [S4]

$$\mathcal{L}_0 = \psi^\dagger \left[i\partial_t + iv_g\partial_z - \frac{1}{2m_0}\partial_z^2 \right] \psi + \frac{1}{m_0 a} \psi^\dagger \psi^\dagger \psi \psi, \quad (\text{S5})$$

$$v_g = \left. \frac{d\epsilon_D(k)}{dk} \right|_{k=k_0}, \quad \frac{1}{m_0} = \left. \frac{d^2\epsilon_D(k)}{dk^2} \right|_{k=k_0}, \quad (\text{S6})$$

where a is the one dimensional scattering length, $\epsilon_D(k)$ is the dispersion relation of the dark-state polaritons obtained from the non-interacting part of \mathcal{H}_{eff} , v_g is the EIT group velocity, and m_0 is the effective mass.

This EFT is exactly solvable in 1D and, for attractive interactions ($a > 0$), it has one N -body bound state for every N [S5, S6]. The properties of the three-body bound state are discussed in the main text. At low-momenta, the lowest order correction to this theory is given by a three-body interaction [S7]

$$\mathcal{L} = \mathcal{L}_0 - V_3, \quad (\text{S7})$$

$$V_3 = \frac{\hbar^3}{36} \psi^\dagger \psi^\dagger \psi^3. \quad (\text{S8})$$

This term, although irrelevant for low-energy, few-body observables in the scaling limit ($|a| \rightarrow \infty$) [S8], has important physical consequences at any finite momentum scale. As discussed in the main text, we can understand the origin of three-body interactions in the Rydberg-EIT system at a qualitative level as arising from the physics of Rydberg blockade. When more than two photons are within a blockade radius from each other, their interaction energy is suppressed due to the blockade effect. This leads to an effective three-body force with the opposite sign from the two-body force as was shown in our recent work [S1] and Ref. [S9]. Although analytic expressions for the three-body interaction were derived in these works, these derivations neglected non-perturbative effects in the renormalization of the microscopic model. In the section below, we provide an alternative estimate of the three-body force that fully accounts for these corrections, but in a simplified version of the microscopic model.

1. Estimating the Three-Body Force

In this section, we outline a procedure to estimate the value of the three-body force in the EFT by matching its prediction for the dimer-polariton scattering length to a simplified version of the microscopic model. Here the dimer is the shallow two-body bound state with the binding energy

$$E_D = -\frac{1}{m_0 a^2}. \quad (\text{S9})$$

Before proceeding to the three-body problem, we first note that the microscopic two-body problem can be solved via an effective Schrödinger equation for a particle with mass m_0 and two-body

interactions of the form [S10, S4]

$$U(\omega, r) = \frac{U(\omega, 0)}{1 + r^6/r_b^6(\omega)}, \quad (\text{S10})$$

$$U(\omega, 0) \approx \frac{\Omega_c^2}{2\Delta} - \omega, \quad (\text{S11})$$

where r is the relative position of the two photons, ω is the total frequency of the incoming photons and the approximate inequality for $U(\omega, 0)$ applies in the experimentally relevant regime of $\Delta \gg (\Omega_c, \Gamma) \gg \gamma_s$. Here we have defined the frequency dependent, complex valued blockade radius $r_b(\omega) = [C_6/U(\omega, 0)]^{1/6}$, which is related to the blockade radius r_B used in the main text and defined in Sec. S1 A through the identity $r_B \approx |r_b(0)|$.

To solve the three-body problem we introduce a simplified description of the full microscopic problem that is easier to treat analytically and numerically. In particular, we replace the effective interaction potential $U(\omega, r)\delta(r - r')$ in the integral equations for the two and three-body scattering amplitudes by a non-local, so-called “separable” potential

$$U(\omega, r, r') = u_0(\omega)u(r)u(r'), \quad (\text{S12})$$

$$u_0(\omega) = \int dr U(\omega, r) = \frac{2\pi}{3} U(\omega, 0) r_b(\omega). \quad (\text{S13})$$

Here r (r') are the relative positions of the two incoming (outgoing) particles in the scattering process. Note that $U(\omega, r, r')$ is not to be confused with $U(r, r')$ defined in Fig. 4(a) of the main text. In our calculations, we take a square well potential in momentum space, i.e., $u(r) = \Lambda \text{sinc}(\pi\Lambda r)$ with $\Lambda \sim 1/r_B$ chosen to match the microscopic two-body scattering length a . The separable approximation allows the two-body T -matrix to be analytically solved and leads to several key simplifications in the implementation of numerical solutions of the Faddeev equations for the three-body scattering amplitudes of Rydberg polaritons [S12].

To fix the value of h_3 we match the dimer-polariton scattering length (obtained numerically) in the EFT to that of the simplified microscopic model. To regularize UV divergences in our solution of the EFT in Eq. (S7), we also take a separable form for the effective two and three-body interactions

$$V_2(r, r') = \frac{2}{m_0 a} v(r)v(r'), \quad (\text{S14})$$

$$V_3(\mathbf{r}, \mathbf{r}') = h_3 v(r_1)v(r_2)v(r'_1)v(r'_2), \quad (\text{S15})$$

where r (r') are the relative coordinate of the two incoming (outgoing) polaritons. For the three-body case, we use the convention that for an incoming polariton with coordinate z_1 and an incoming dimer with coordinates (z_2, z_3) , $r_1 = z_1 - z_2$ and $r_2 = z_1 - z_3$ and similarly for the outgoing coordinates. In the EFT we take a square well potential in real space $v(r) = \theta(\delta r - |r|)/2\delta r$ with $\theta(\cdot)$ the Heaviside step function. The potential is chosen as a square well because this is the form we use for the interactions when solving the transmission problem using the EFT. Defining the interaction parameter $\varphi = \text{OD}_B \Gamma / 4\Delta = g^2 r_B / c\Delta$, we parameterize the range of the effective potentials as $\delta r = \alpha r_B / \varphi$ for $\alpha \lesssim 1$. Since the scattering length in the

experimentally relevant regime of small φ satisfies $a \approx r_B/\varphi^2$ [S4], we have $\delta r/a \approx \alpha\varphi \ll 1$, such that these potentials can be well approximated by contact interactions at low-momentum. To perform the matching, we fix $h_3 m_0 = \beta\varphi^2$ for some choice of β and then adjust the range of the potential via α to match the scattering amplitudes. For Fig. 4 in the main text we chose $\beta = 13.5$ near the value obtained from our previous analytic predictions for the three-body force [S1, S9]. Performing the matching calculation we found $\alpha \approx 0.1$ for the experimentally relevant range of φ . Although the precise choice of matching procedure is somewhat arbitrary, what is important is that the physical observables are independent of these details. We have verified that the predicted values of the ratio $\phi_3(0,0)/\phi_2(0)$ from the EFT vary by less than 5 % when the choice of β , with α obtained from matching, is varied within 50 %.

2. Comparison Between EFT, Numerical Simulations, and Experimental Data

To solve the transmission problem we use a modified version of the EFT that takes into account the spatial inhomogeneity of the atomic density. Most notably, we use a local density approximation (i.e., each parameter is defined in terms of the local value of $g(z)$) and transform into a moving frame through the coordinate transformation [S1]

$$\bar{z} = t - \int_0^z dz' \frac{1}{v_g(z')}, \quad (\text{S16})$$

$$\tau = z, \quad (\text{S17})$$

which transforms the Lagrangian to the form

$$\mathcal{L} = \psi^\dagger \left[i v_g(\tau) \partial_\tau - \frac{\partial_{\bar{z}}^2}{2m_0(\tau)v_g^2(\tau)} \right] \psi + \frac{\psi^{\dagger 2} \psi^2}{m_0(\tau)a(\tau)v_g(\tau)} - \frac{h_3(\tau)}{36 v_g^2(\tau)} \psi^{\dagger 3} \psi^3, \quad (\text{S18})$$

where we have rescaled the field $\psi(z) \rightarrow \psi(\bar{z})/\sqrt{v_g(\tau)}$ such that $[\psi(\bar{z}), \psi^\dagger(\bar{z})] = \delta(\bar{z} - \bar{z}')$ and we have neglected higher-order derivatives involving ∂_τ as their effect is suppressed due to the presence of the linear time derivative. This EFT is a more convenient formulation of the transmission problem because the parameters now depend on “time” τ , which only appears with a single derivative. As a result, this theory can be solved by treating it as a time-dependent Hamiltonian problem. Furthermore, it illustrates that the transmission through the medium can be mapped to a quantum quench, where the duration of the time evolution following the quench is given by the EIT group delay $\tau_d = \int dz \frac{1}{v_g(z)}$ [S1, S10, S14]. When numerically solving for the transmission using Eq. (S18), we regularize the two and three-body contact interactions by taking symmetrized, local and non-separable square well interaction potentials

$$V_2(\bar{z}_i, \bar{z}_j) = \frac{2}{m_0 a} v(\bar{z}_i - \bar{z}_j), \quad (\text{S19})$$

$$V_3(\bar{z}_1, \bar{z}_2, \bar{z}_3) = \frac{h_3}{3} [v(\bar{z}_1 - \bar{z}_2)v(\bar{z}_1 - \bar{z}_3) + v(\bar{z}_1 - \bar{z}_2)v(\bar{z}_2 - \bar{z}_3) + v(\bar{z}_1 - \bar{z}_3)v(\bar{z}_2 - \bar{z}_3)], \quad (\text{S20})$$

where $v(r) = \theta(\delta r - |r|)/2\delta r$, $h_3 = \beta\varphi^2/m_0$, $\delta r = \alpha r_B/\varphi$ and α and β were determined via the matching procedure for separable potentials described in the previous section. In contrast

to the separable potentials defined in Eq. (S14)-(S15), here we have suppressed the dependence on the outgoing coordinates as, due to the locality assumption, the outgoing coordinates are constrained to be equal to the incoming coordinates.

In Fig. S3(a-b) we compare the predictions from numerical solutions of Eq. (S18) for the transmission through a finite medium to full numerical simulations that account for the microscopic form of the Rydberg interactions [S15]. We see good agreement between the numerics and the EFT at intermediate times. The deviations at short times are due to the breakdown of the low-energy assumption and the deviations at long times arise from the finite length of the medium [S1]. We use the initial condition outside the medium of a uniform state with unit amplitude. We find that including the three-body interaction improves the agreement with $\phi_3(t, 0)$ at intermediate times. Similar to Fig. 3 in the main text, we see that including the three-photon force reduces the ratio $\phi_3(0, 0)/\phi_2(0)$, where $\phi_2(t)$ is the two-photon phase. Table S1 shows the ratio $\phi_3(0, 0)/\phi_2(0)$ for the three different models, where we see that including the three-body force is able to account for the deviation of this ratio below 3. Despite the disagreement between the values of $\phi_3(t, 0)$ in the simulations and the EFT at short times seen in Fig. S3, we find that the ratio $\phi_3(t, 0)/\phi_2(t)$ is roughly independent of t near the origin, which justifies the comparison.

In Table S2 we compare the theoretical predictions from the EFT and the simulations against the measured values of $\phi_3(0, 0)/\phi_2(0)$ from Fig. 4 in the main text. Here $\langle \varphi \rangle = \tau_d^{-1} \int dz \varphi(z)/v_g(z)$ is the average value of $\varphi(z) = \text{OD}_B \Gamma / 4\Delta = g^2(z)r_B/c\Delta$ weighted by the time spent in each region. As mentioned in the main text, we fit the two-photon detuning δ within the experimental uncertainty $\delta/2\pi = 0.0 \pm 0.5$ MHz by matching the measured value of $\phi_2(0)$ to the simulations. All other parameters are determined from independent measurements without fitting. Although $\phi_2(0)$ and $\phi_3(0, 0)$ are sensitive to the precise value of δ , we find that the theoretical prediction for the ratio $\phi_3(0, 0)/\phi_2(0)$ varies by less than 5 % when varying δ within the experimental uncertainty. We see that the EFT with the three-body force gives good agreement with both the data and the simulations, while we can clearly rule out the EFT without the three-body force.

C. Formation of N -Body Bound States

In this section we present a general argument that the propagation through the medium leads to the formation of an N -body bound state near zero time delay between the polaritons. We first consider the two-body problem in a uniform medium. Defining the center of mass $R = (z_1 + z_2)/2$ and relative $r = z_1 - z_2$ coordinates for the two polaritons, we expand the wavefunction in the eigenbasis of the EFT given in Eq. (S5) [S10]

$$\psi(t, R, r) = c_b e^{-|r|/a - iE_D t} + \int_0^\infty \frac{dq}{2\pi} c_q \psi_q(r) e^{-iq^2 t/m_0}, \quad (\text{S21})$$

where the first term is the dimer wavefunction, $\psi_q(r) = (e^{iq|r|} + b_q e^{-iq|r|})/\sqrt{2}$ is the wavefunction for the two-body scattering states, $b_q = (iaq + 1)/(iaq - 1)$, and we work in the center of mass

frame so that $\partial_R \psi = 0$. The coefficients c_b and c_q are determined by initial conditions.

For a long medium, we can find the transmission analytically for $|r|/a \ll \sqrt{|E_D t|}$ using a saddle point expansion

$$\psi(t, R, r) \approx c_b e^{-|r|/a - iE_D t} + O(|E_D t|^{-1/2}), \quad (\text{S22})$$

where the second term is due to the contribution from scattering states. The condition to neglect the second term for the transmitted light is

$$\tau_d |E_D| \approx 2\varphi^2 \text{OD} \Gamma / \Delta \gg 1, \quad (\text{S23})$$

where τ_d is the EIT group delay defined in Sec. S2B2. From this analysis we see that the dispersive nature of the scattering states results in the bound state dominating the transmission near the origin in the off-resonant, high OD limit.

To see how this argument generalizes to $N > 2$, we move to a relative coordinate system r_1, \dots, r_{N-1} (defined as any set of coordinates orthogonal to the center of mass coordinate $R = \sum_i z_i / N$). The general form for the evolution in the center of mass frame is given by

$$\psi(t, R, \mathbf{r}) = c_b \psi_b(\mathbf{r}) e^{-iE_N t} + \int \frac{dq}{2\pi} c_{bq} \psi_{bq}(\mathbf{r}) e^{-iE_{N-1} t - iq^2 t / 2m_0} + \dots, \quad (\text{S24})$$

where ψ_b is the wavefunction for the N -body bound state, $\psi_{bq}(\mathbf{r})$ is the wavefunction for a combined $(N-1)$ -body bound state and a scattering state with relative momentum q , etc. Similar to the two-body problem, we can see that all contributions to ψ besides ψ_b will dephase with each other. As a result, the transmission is dominated by the bound state near the origin.

For the experiments studied in this work, $|E_N| \gtrsim \tau_d^{-1}$, therefore, it is important to also take into account the contributions from the scattering states in solving the transmission problem. To include these contributions when modeling the experiments, we perform numerical simulations of the two and three-photon wavefunction propagation equations derived from the EFT in Eq. (S18) including the inhomogeneous density profile.

D. Finite Rate Corrections to Theory

The correlation functions analyzed above were taken with respect to the vacuum. In the experiment, the input state is a coherent state, which implies that N -particle correlation functions contain contributions from higher and lower particle-number manifolds. In the limit of a long coherent state pulse with a finite photon rate R , we now evaluate these corrections perturbatively in the normalized polariton density $R\tau_{\text{int}}$. Here $\tau_{\text{int}} \sim \tau_d$ is defined as the relative time difference over which the correlation functions do not factorize. We show that these finite rate corrections are small, which justifies our approximation of neglecting these corrections when comparing our theory to experimental data.

We write the input state as

$$e^{\alpha^2/2} |\mathcal{E}\rangle = |0\rangle + \alpha |1\rangle + \frac{\alpha^2}{\sqrt{2!}} |2\rangle + \frac{\alpha^3}{\sqrt{3!}} |3\rangle + \dots, \quad (\text{S25})$$

where

$$|n\rangle = \frac{(a^\dagger)^n}{\sqrt{n!}}|0\rangle, \quad a^\dagger = \frac{1}{\sqrt{T}} \int dz \mathcal{E}(z) \psi_g^\dagger(z). \quad (\text{S26})$$

Here $\mathcal{E}(z)$ is our input mode which we take to be a long uniform pulse of unit amplitude and duration T from $z = 0$ to $z = T$ ($c=1$). We write the output as

$$\begin{aligned} e^{\alpha^2/2}|\mathcal{E}\rangle &= |0\rangle + \sqrt{R} \int dz \mathcal{E}_1(z) \psi_g^\dagger(z) |0\rangle + \frac{R}{2} \int dz_1 dz_2 \mathcal{E}_2(z_1, z_2) \psi_g^\dagger(z_1) \psi_g^\dagger(z_2) |0\rangle \\ &+ \frac{R^{3/2}}{6} \int dz_1 dz_2 dz_3 \mathcal{E}_3(z_1, z_2, z_3) \psi_g^\dagger(z_1) \psi_g^\dagger(z_2) \psi_g^\dagger(z_3) |0\rangle + \dots, \end{aligned} \quad (\text{S27})$$

where the input photon rate is $R = \alpha^2/T$ and we define g_n and ϕ_n via

$$\mathcal{E}_n(z_1, \dots, z_n) = \sqrt{g_n(z_1, \dots, z_n)} e^{i\theta_n(z_1, \dots, z_n)}. \quad (\text{S28})$$

Notice that g_n and θ_n are different from the measured $g^{(n)}$ and ϕ_n because of the rate-dependent corrections. Neglecting dissipation leads to the normalization condition

$$e^{\alpha^2} = e^{\alpha^2} \langle \mathcal{E} | \mathcal{E} \rangle = 1 + R \int dz_1 g_1(z_1) + \frac{R^2}{2} \int dz_1 dz_2 g_2(z_1, z_2) + \dots, \quad (\text{S29})$$

which requires the identity

$$\int d^n z [g_n(z_1, \dots, z_n) - 1] = 0. \quad (\text{S30})$$

One can show that including the decay rates in the effective Hamiltonian gives the leading order contribution to this integral on the order of $(\Gamma/\Delta)\tau_{\text{int}}^n$.

These identities allow us to prove that g_n converges to $g^{(n)}$ in the limit of vanishing input rate $R\tau_{\text{int}} \rightarrow 0$. For example, for g_2 we find

$$\begin{aligned} g^{(2)}(z_1, z_2) &= \frac{1}{R^2} \langle \mathcal{E} | \psi_g^\dagger(z_1) \psi_g^\dagger(z_2) \psi_g(z_2) \psi_g(z_1) | \mathcal{E} \rangle \\ &= e^{-\alpha^2} [g_2(z_1, z_2)(1 + \alpha^2 + \dots) + R \int dz [g_3(z_1, z_2, z) - g_2(z_1, z_2)] + \dots], \end{aligned} \quad (\text{S31})$$

Collecting all terms that are zeroth order in $R\tau_{\text{int}}$, we recover $g_2(z_1, z_2)$. In the limit $\Delta \gg \gamma$, this analysis also gives access to the first order correction in $R\tau_{\text{int}}$, which takes the general form

$$\begin{aligned} g^{(n)}(\tau_1, \dots, \tau_{n-1}) &= g_n(\tau_1, \dots, \tau_{n-1}) \\ &+ R \int d\tau (g_{n+1}(\tau_1, \dots, \tau_{n-1}, \tau) - g_n(\tau_1, \dots, \tau_{n-1})). \end{aligned} \quad (\text{S32})$$

For the single-photon phase, we can follow similar arguments to find

$$\frac{1}{\sqrt{R}} \langle \mathcal{E} | \psi_g(z) | \mathcal{E} \rangle = e^{i\theta_1} + R \int d\tau (\sqrt{g_2(\tau)} e^{i(\theta_2(\tau) - \theta_1)} - e^{i\theta_1}) + O(R^2 \tau_{\text{int}}^2), \quad (\text{S33})$$

and, generalizing to ϕ_n ,

$$\begin{aligned} &\frac{1}{R^{n-1/2}} \langle \mathcal{E} | \psi_g^\dagger(z_1) \dots \psi_g^\dagger(z_{n-1}) \psi_g(z) \psi_g(z_{n-1}) \dots \psi_g(z_1) | \mathcal{E} \rangle \\ &= \mathcal{E}_{n-1}^*(z_1, \dots, z_{n-1}) \mathcal{E}_n(z_1, \dots, z_{n-1}, z) \\ &+ R \int dz' [\mathcal{E}_n^*(z', z_1, \dots, z_{n-1}) \mathcal{E}_{n+1}(z', z_1, \dots, z_{n-1}, z) \\ &- \mathcal{E}_{n-1}^*(z_1, \dots, z_{n-1}) \mathcal{E}_n(z_1, \dots, z_{n-1}, z)]. \end{aligned} \quad (\text{S34})$$

Using these formulas, we have explicitly evaluated the rate dependent corrections to ϕ_2 and ϕ_3 by numerically solving the four-photon transmission problem within the EFT. The results are shown in Fig. S4. For this data set ($\Delta/2\pi = 30$ MHz), the experiments were performed at a rate near 1 photon/ μs . In this regime, the rate dependent corrections to the phase ratio are on the order of a few percent. This mostly rules out the rate dependent corrections as an explanation for the deviation of the phase ratio from three observed in the experiment. We find similar results for the other data sets. In Fig. 4B of the main text we compare the zero-rate predictions of the EFT to the experimentally measured values of $\phi_3(0,0)/\phi_2(0)$. In Fig. 4B of the main text we compare the zero-rate predictions of the EFT to the experimentally measured values of $\phi_3(0,0)/\phi_2(0)$.

E. Dissipative Corrections to Theory

At large single-photon detunings Δ the dominant decay is due to the finite decoherence rate $\gamma_s/2$ of the Rydberg state. Experimentally we observe that the single-photon transmission through the medium is between 50 % and 90 %. Although we include the decay terms in the non-Hermitian Hamiltonian evolution, this large background decay inside the medium raises the question of whether we are justified in neglecting the recycling terms in the master equation. As was argued in Sec. S2 A, this approximation is indeed justified at sufficiently low polariton densities. More precisely, we find the requirement to neglect the recycling terms is given by $\gamma_s\tau_d R\tau_{\text{int}} \ll 1$. This condition is well satisfied for the experiment even when $\gamma_s\tau_d \sim 1$, which justifies our theoretical approach in which we neglect these corrections when comparing to experimental data.

We do not give a detailed proof of this result here, but note that this scaling can be understood intuitively because $\gamma_s\tau_d$ is the expected number of decay events, or “quantum jumps,” per photon during the transmission through the medium, while $R\tau_{\text{int}}$ is the probability of having a second photon within the interaction range of the first when the quantum jump occurs, i.e., the normalized polariton density. Thus, under the condition $\gamma_s\tau_d R\tau_{\text{int}} \ll 1$, the quantum jumps typically happen when there are no other polaritons nearby with which to interact. In this case, the interacting correlation functions will have a small contribution from quantum jump events from higher excitation number manifolds.

The role of quantum jumps associated with other loss processes inside the medium requires a separate treatment from the Rydberg decay because these effects appear in the polariton dynamics as momentum or frequency dependent loss (e.g., an imaginary mass term). In this case, the argument above does not apply because, for a long uniform pulse that has reached steady state inside the medium, these loss processes are always correlated with interactions between the polaritons. As a result, these quantum jump events do not average out when evaluating interacting correlation functions. It is not difficult to show, however, that these corrections are suppressed as the product of two small parameters $R\tau_{\text{int}}$ and Γ/Δ , which justifies our neglect

of these quantum jump processes.

-
- [S1] M. J. Gullans, J. D. Thompson, Y. Wang, Q.-Y. Liang, V. Vuletić, M. D. Lukin, and A. V. Gorshkov, Phys. Rev. Lett. **117**, 113601 (2016).
 - [S2] T. Peyronel, O. Firstenberg, Q.-Y. Liang, S. Hofferberth, A. V. Gorshkov, T. Pohl, M. D. Lukin, and V. Vuletic, Nature **488**, 57 (2012).
 - [S3] H. Carmichael, R. Brecha, and P. Rice, Opt. Commun. **82**, 73 (1991).
 - [S4] P. Bienias, S. Choi, O. Firstenberg, M. F. Maghrebi, M. Gullans, M. D. Lukin, A. V. Gorshkov, and H. P. Büchler, Phys. Rev. A **90**, 053804 (2014).
 - [S5] E. H. Lieb and W. Liniger, Phys. Rev. **130**, 1605 (1963).
 - [S6] J. B. McGuire, J. Math. Phys. **5**, 622 (1964).
 - [S7] E. Braaten and H. W. Hammer, Phys. Rep. **428**, 259 (2006).
 - [S8] S. K. Adhikari, T. Frederico, and I. D. Goldman, Phys. Rev. Lett. **74**, 487 (1995).
 - [S9] K. Jachymski, P. Bienias, and H. P. Büchler, Phys. Rev. Lett. **117**, 053601 (2016).
 - [S10] O. Firstenberg, T. Peyronel, Q.-Y. Liang, A. V. Gorshkov, M. D. Lukin, and V. Vuletić, Nature **502**, 71 (2013).
 - [S11] A. V. Gorshkov, J. Otterbach, M. Fleischhauer, T. Pohl, and M. D. Lukin, Phys. Rev. Lett. **107**, 133602 (2011).
 - [S12] M. J. Gullans *et al.* in preparation.
 - [S13] P. F. Bedaque, H.-W. Hammer, and U. van Kolck, Phys. Rev. Lett. **82**, 463 (1999).
 - [S14] P.-É. Larré and I. Carusotto, Phys. Rev. A **92**, 043802 (2015).
 - [S15] M. J. Gullans, PhD Thesis, Harvard University, Cambridge, MA (2013).

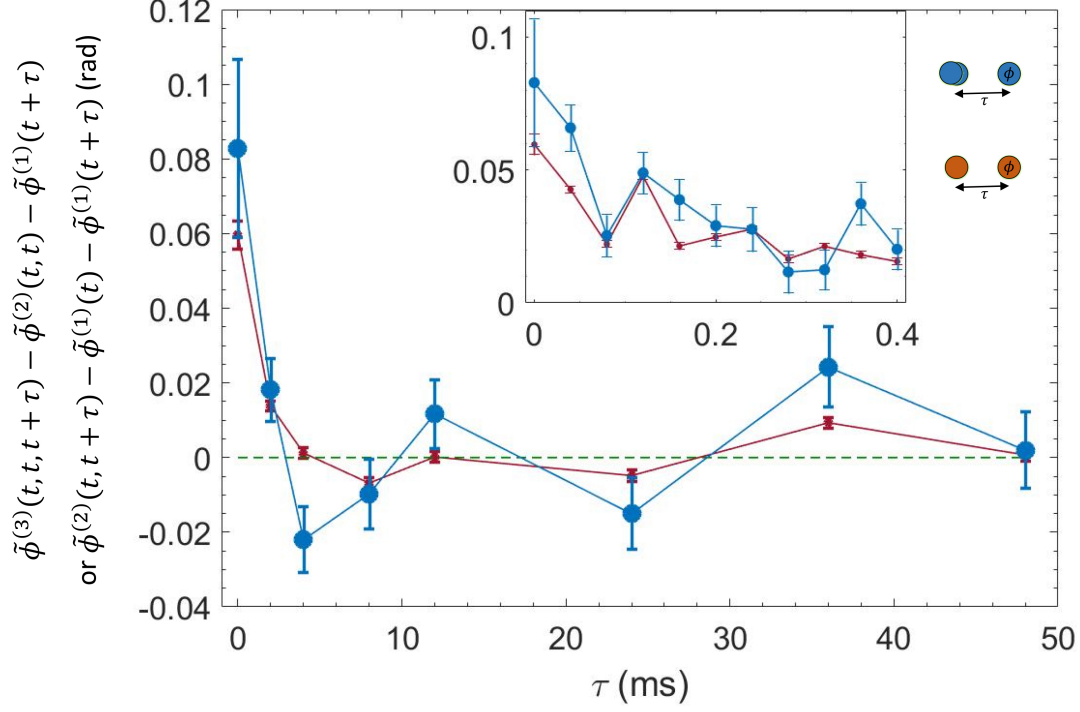


FIG. S1: **The long range behavior of the conditional phase referenced to the local unconditional phase.** The blue and brown data represent $\tilde{\phi}^{(3)}(t, t, t + \tau) - \tilde{\phi}^{(2)}(t, t) - \tilde{\phi}^{(1)}(t + \tau)$ and $\tilde{\phi}^{(2)}(t, t + \tau) - \tilde{\phi}^{(1)}(t) - \tilde{\phi}^{(1)}(t + \tau)$, respectively. The inset shows the same quantities at a shorter time scale. These data with τ much longer the probe pulse ($\sim 6\mu\text{s}$) are generated by taking detection events from different pulses. Data is the same as in Fig. 3 of the main text.

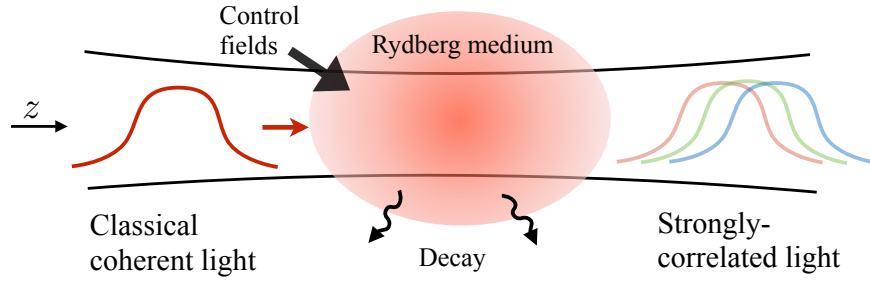


FIG. S2: **The scheme of the experiment.** This experiment can be conceptualized as a multi-particle transport problem whereby a classical coherent pulse of light enters the medium and becomes strongly-correlated on the output due to strong coherent and dissipative interactions inside the medium.

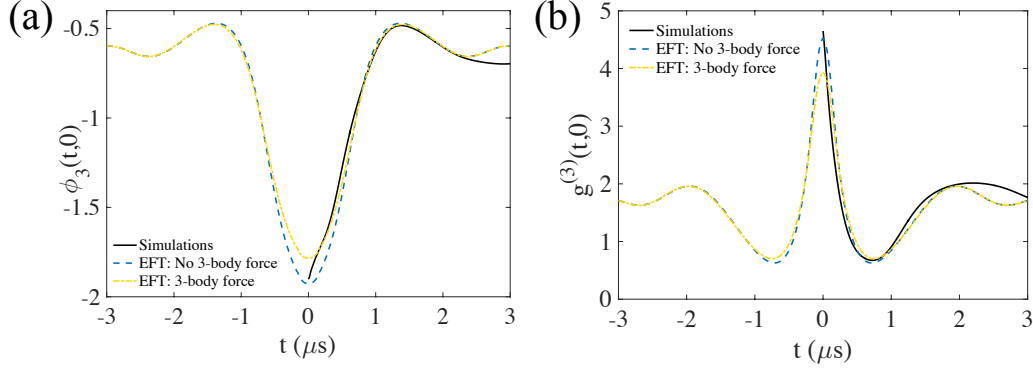


FIG. S3: **Comparison between EFT and simulations.** We compare the EFT predictions for the two and three photon transmission through a finite medium (see Ref. [S1]) and numerical simulations for (a) the three-photon phase $\phi_3(t,0)$ and (b) the three-photon amplitude $g^{(3)}(t,0)$. Here we took parameters similar to the current experiments, but with a uniform density profile of length $144 \mu\text{m}$, a resonant $\text{OD}=68$, $\Omega_c/2\pi = 5 \text{ MHz}$, $\Delta = 30 \text{ MHz}$, $\gamma_s = 0$, and $r_B = 10 \mu\text{m}$.

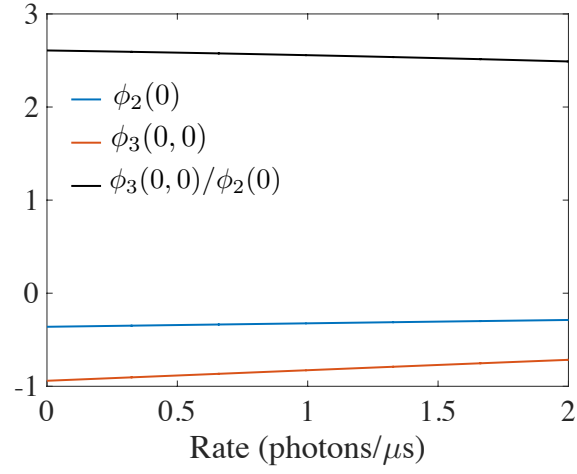


FIG. S4: **Rate dependent corrections within the EFT.** We use parameters from the 30 MHz data set. The experiment for this data set was performed at a rate of 1 photon/ μ s.

Model	$\phi_3(0,0)/\phi_2(0)$
Simulations	2.90
EFT: No 3-body force	3.13
EFT: 3-body force	$2.85 \pm .11$

TABLE S17: **Comparison of phase ratio between EFT and simulations.** Comparison for the prediction of the phase ratio near zero time delay between different models for parameters as in Fig. S3. The uncertainty in the EFT with the three-body force arises from the variations with the choice of matching conditions for the dimer-polariton scattering length.

$\langle\varphi\rangle=\langle\text{OD}_B\rangle\Gamma/4\Delta$	0.16	0.21	0.28	0.36	0.47
Measured $\phi_3(0,0)/\phi_2(0)$	$2.17 \pm .18$	$2.45 \pm .15$	$2.55 \pm .13$	$2.33 \pm .27$	$2.31 \pm .21$
EFT: 3-body force	$2.64 \pm .18$	$2.42 \pm .17$	$2.48 \pm .11$	$2.60 \pm .11$	$2.52 \pm .13$
Simulations	2.77	2.66	2.72	2.63	2.60
EFT: No 3-body force	3.06	3.05	3.07	3.08	3.06
Fitted δ ($2\pi\cdot\text{MHz}$)	0.6	0.6	0	-0.2	-0.4

TABLE S18: **Comparison of phase ratio between EFT, simulations and experimental data.**

Comparison of measured $\phi_3(0,0)/\phi_2(0)$ presented in Fig. 4B of the main text to predictions from EFT with and without the three-body force and the simulations [S15]. We took an inhomogeneous Gaussian density profile with $\sigma_{\text{ax}} = 32 \mu\text{m}$, $\gamma_s/2\pi = 200 \text{ kHz}$, δ as shown (obtained from fitting the measured value of $\phi_2(0)$ to the simulations), and other parameters as given in the main text. The uncertainty in the EFT with the three-body force arises from the variations with the choice of matching conditions for the dimer-polariton scattering length.